

# X-RAY IMAGING AND SPECTROSCOPY OF THE SUPERNOVA REMNANT CTB 109 AND ITS ASSOCIATED PULSAR 1E 2259 + 586

JEONGHEE RHO<sup>1</sup>

NASA/Goddard Space Flight Center; and Service d'Astrophysique, CEA, Centre d'Etudes de Saclay,  
 F-91191 Gif-sur-Yvette, France

AND

R. PETRE

Code 662, NASA/Goddard Space Flight Center, Greenbelt, MD 20771

Received 1996 April 10; accepted 1997 February 27

## ABSTRACT

We present the results of our analysis of the X-ray spectral structure of the evolved supernova remnant CTB 109 (G109.1–1.0), using data from the *ROSAT* Position Sensitive Proportional Counter (PSPC) and Broad Band X-Ray Telescope (BBXRT). The deep broadband PSPC image shows the same overall remnant morphology as previous X-ray images but reveals many new details. The remnant appears as a hemispherical shell centered on the X-ray–bright central pulsar 1E 2259 + 586. Despite the substantial improvement in sensitivity of the PSPC image over previous images, no X-ray emission is detected from the western half of the remnant, consistent with the interpretation that the western shock front has been significantly decelerated by a dense molecular cloud. Enhanced emission along the cloud remnant boundary supports this interpretation. Among important new small-scale structures revealed are clumpy substructure within the jetlike lobe running northeastward from the pulsar to the shell, and extended emission, with 2–3 arc minute radius, around 1E 2259 + 586.

Spatially resolved spectroscopy using the PSPC reveals an overall column density variation across the remnant as well as intrinsic spectral variations. In particular, the spectrum over most of the shell is well fitted by a single-component thermal model, while for the lobe, the northern and southern shell, two thermal components are required, with one having parameter values similar to that found in those regions fitted by a single-component model. We conclude that either the thermal conditions vary within the remnant or there exists a second, distinct gas component in some parts of the remnant. A simultaneous fit to BBXRT and PSPC spectra for part of the interior and shell to the south of the pulsar shows that the plasma there is not in ionization equilibrium. The results of fitting these spectra using nonequilibrium ionization models are ambiguous, however: equally acceptable fits were obtained using models with and without electron-ion equipartition, but with very different parameter values. The best non-equipartition model yields shock temperature  $T_s = 2 \times 10^7$  K and ionization parameter  $n_0 t = 430 \text{ cm}^{-3} \text{ yr}$ , suggesting extreme departure from ionization equilibrium, while the best-fit equipartition model indicates conditions near ionization equilibrium, with  $T_s = 1.8 \times 10^6$  K and  $n_0 t = 17,000 \text{ cm}^{-3} \text{ yr}$ .

The thermal nature of the emission from the lobe is counter to the prediction of the hypothesis that it arises from a precessing jet and contrasts with the nonthermal lobes in SS433/W50. Thus, the lobe in CTB 109 is probably not related to or powered by the central pulsar. The similarity of the lobe spectrum to those of the northern and southern shell segments suggests they are physically related. Together they form a plumelike structure whose morphology and location relative to the molecular cloud suggest that they represent gas from the remnant interior, swept up and reheated by a shock reflected off the molecular cloud, as reproduced in hydrodynamical simulations (see Tenorio-Tagle et al.).

A timing analysis of the PSPC data for 1E 2259 + 586 yields a period of  $6.978814 \pm 9.4 \times 10^{-6}$  s, consistent with a constant  $\dot{P}$ . Simultaneous fitting of the pulsar spectra from the PSPC, BBXRT, and the *ASCA* are best modeled by a blackbody ( $kT = 0.43$  keV).

The extended emission around 1E 2259 + 586 has an extent of 2'–3' in both the PSPC and *ROSAT* HRI images. Its nonthermal spectrum suggests that it arises from a synchrotron nebula, although we cannot rule out the possibility of a dust-scattering halo.

*Subject headings:* ISM: individual (CTB 109) — pulsars: individual (PSR 1E 2259 + 586) — supernova remnants — X-rays: ISM

## 1. INTRODUCTION

CTB 109 (G109.1–1.0) is a “composite” supernova remnant (SNR) in the X-ray band, containing both a central point source and a shell. Other remnants in this category

are Vela and CTB 80. The remnant CTB 109 has a semi-circular shape, with a hemispherical eastern shell centered on the X-ray–bright central pulsar 1E 2259 + 586. No X-ray or radio shell has been detected from the western hemisphere. The central pulsar is a very strong X-ray source but has no radio counterpart (Gregory & Fahlman 1980). Neither X-ray nor radio observations to date have suggested any evidence of a synchrotron nebula. A surface

<sup>1</sup> Send offprint requests to jrho@discovery.saclay.cea.fr.

brightness enhancement, a “lobe,” connects the pulsar and the northeastern shell; this feature has been referred to as an “X-ray jet” (Gregory & Fahlman 1980).

The remnant is located in a complicated region of the Galaxy, with a giant molecular cloud to the west, containing five H II regions: S147, S148, S149, S152, and S153. The CO map (Tatematsu et al. 1987) and *IRAS* observations (Heydari-Malayeri, Kahane, & Lucas 1981) suggest that the western portion of the shell is missing as a result of the interaction between the SNR and the molecular cloud. There is massive star formation activity in the molecular cloud. There are arms in CO emission stretching from the molecular cloud across the SNR in both the northern and southern parts of the remnant. A velocity shift ( $2\text{--}4\text{ km s}^{-1}$ ) is reported along the northern arm, indicating that the arm material has been accelerated by the SNR shock (Tatematsu et al. 1985). In contrast to the H I shell expanding at  $90\text{ km s}^{-1}$  (Giovanelli & Haynes 1979) and shock-accelerated CO gas with a velocity dispersion of  $20\text{ km s}^{-1}$  found in IC 443, another SNR strongly interacting with a molecular cloud, no high-velocity H I or broad lines have been found in CTB 109 (Tatematsu et al. 1987).

The central pulsar, 1E 2259 + 586, has an approximately 6.98 s period and a small positive period derivative ( $\dot{P} = 3.2 \times 10^{-6}\text{ yr}^{-1}$ ; see Koyama, Hoshi, & Nagase 1987; Morini et al. 1988; Koyama et al. 1989). It has a rotational energy loss rate of  $10^{32}\text{ ergs s}^{-1}$ , assuming it is a neutron star, and a 1.2–20 keV luminosity of  $1.2 \times 10^{35}\text{ ergs s}^{-1}$  (Koyama et al. 1989). A possible optical counterpart has been proposed based on IR and optical pulsations (Fahlman, & Hickson, & Richer 1982; Middleditch, Penypacker, & Burns 1983). However, a recent IR observation did not detect pulsations (Davies et al. 1989). *EXOSAT* observations suggest that the pulsar might not be in a binary system, since no evidence for a companion has been found (Morini et al. 1988). The curled jetlike X-ray structure (or lobe) has been proposed to originate from the pulsar (Gregory & Fahlman 1983; Manchester 1987) or to be related to the molecular cloud (Tatematsu et al. 1987). Tatematsu et al. suggest that the CO ridge to the north and west of the lobe is physically related to it: the high molecular column density of the ridge absorbs the X-ray emission to the north of the lobe, creating the artificial appearance of an X-ray enhancement.

The radio spectral index  $\alpha$  of CTB 109 [where  $S(\nu) \propto \nu^{-\alpha}$  using  $\lambda = 4.6\text{--}49\text{ cm}$ ] is  $0.5 \pm 0.04$  (Hughes et al. 1984) and does not vary across the SNR. The optical spectrum has strong [S II]  $\lambda\lambda 6717$  and  $6731$  relative to H $\alpha$ , indicating the presence of shock-heated gas. A few optical filaments are observed in the northeastern and southern shell (Hughes et al. 1981). The spectroscopic distances for the exciting stars of the nearby H II regions are estimated to be 3.6–5.5 kpc, and the  $\sigma$ -D relation gives 4.1 kpc (Sofue, Takahara, & Hirabayashi 1983) and 5.6 kpc (Hughes et al. 1984) for CTB 109. We assume here 4 kpc as the distance to CTB 109.

In this paper, we focus upon the physical conditions of the diffuse X-ray emission of CTB 109. We present temperature and column density maps, obtained from spatially resolved spectral fitting. Nonequilibrium ionization (NEI) models have been used to fit Broad Band X-Ray Telescope (BBXRT) and Position Sensitive Proportional Counter (PSPC) spectra, and the implications of these are given. We also report our discovery of extended emission around 1E 2259 + 586. This paper is organized as follows. In § 2, we

describe the *ROSAT* PSPC and BBXRT observations. In § 3 the X-ray images of CTB 109 are presented and compared with other wavelength images, and the results of spectral fitting are summarized. We also briefly discuss the characteristics of the pulsar 1E 2259 + 586 as inferred from the PSPC, BBXRT, and *Advanced Satellite for Cosmology and Astrophysics (ASCA)* data. In § 4, we discuss the properties and origin of X-ray gas in CTB 109 and its relationship to the interaction with the molecular cloud.

## 2. OBSERVATIONS

### 2.1. *ROSAT* Observation

CTB 109 was observed using the *ROSAT* PSPC on 1991 July 9–10. The exposure time is 34,000 s, and the total source count rate is  $9.36 \pm 0.02\text{ counts s}^{-1}$ . The pointing position is R.A. =  $23^{\text{h}}01^{\text{m}}24^{\text{s}}$  and decl. =  $58^{\circ}53'16''$  (J2000). The data presented here have been extracted from the *ROSAT* archive. The angular size of CTB 109,  $28' \times 34'$ , allowed it to be viewed entirely within the central  $40'$  diameter area of the PSPC, where spatial variations of the point response function and energy-dependent vignetting are minimal. The PSPC image has been precessed to epoch 1950 to facilitate comparison with other images, and is displayed as epoch 1950 unless otherwise specified.

We also have used data from a *ROSAT* HRI observation, for comparison between the pulsar 1E 2259 + 586 radial profile and the HRI point-spread function (PSF). This observation took place 1992 January 8–10 and has an exposure time of 22,320 s.

### 2.2. *BBXRT* Observation

The BBXRT was an instrument designed to perform high-sensitivity, moderate-resolution spectroscopy (12% at 1 keV) over the energy range 0.3–10 keV as part of the *Astro-1* payload on the Space Shuttle Columbia. A detailed description of the instrument can be found in Serlemitsos et al. (1992). There are two identical detectors (A and B), each of which was divided into a central, circular element (with a field of view 4/5 in diameter), and four outer quadrants extending the field of view to 17/4 (see Fig. 6a below). The observation took place on 1990 December 5, and the exposure time is 2240 s. The diffuse emission was observed in the outer pixel pairs A3/B1 and A4/B2, whose count rates without background subtraction are 0.54/0.41  $\text{counts s}^{-1}$  and 0.50/0.32  $\text{counts s}^{-1}$ , respectively. The spectral resolution of these pixels are approximately 110 eV at 1 keV and approximately 170 eV at 6 keV. Background subtraction has been applied for spectral fitting. The channels below 0.6 keV and above 10 keV are not included.

## 3. RESULTS

### 3.1. *X-Ray Image and Hardness Map*

The PSPC image is shown in Figure 1. It was produced by smoothing the raw data with a Gaussian convolving function with  $\sigma = 15''$ . The contours are  $2.35 \times 10^{-3}\text{--}0.14\text{ counts s}^{-1}\text{ arcmin}^{-2}$ . The difference between adjacent contours is a multiplicative factor of 1.17. While qualitatively similar to the *Einstein* IPC and *EXOSAT* images, the higher spatial resolution and signal-to-noise ratio of the PSPC image reveals many more fine details. The X-ray emission is confined to an approximately hemispherical shell centered upon 1E 2259 + 586. While low surface

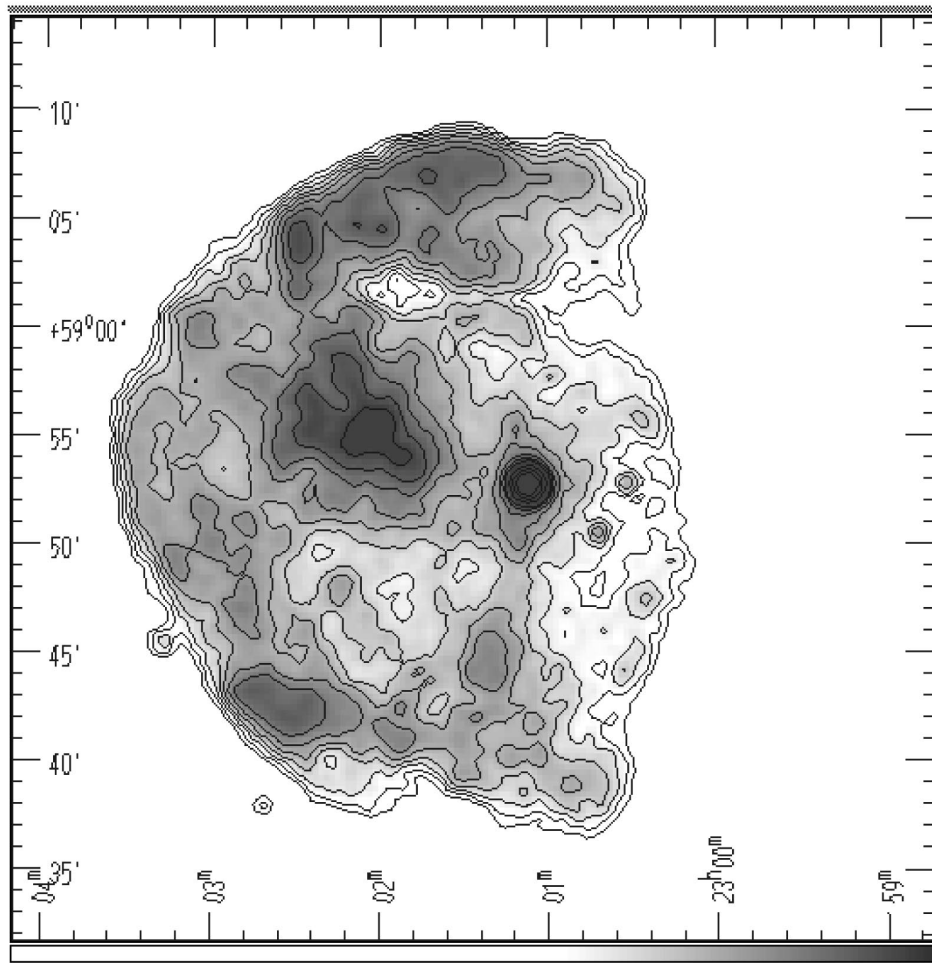


FIG. 1.—The smoothed *ROSAT* PSPC image of CTB 109. Coordinates are J2000. The contours are  $2.35 \times 10^{-3}$  to  $0.14 \text{ counts s}^{-1} \text{ arcmin}^{-2}$ . The difference between adjacent contours is a multiplicative factor of 1.17. The maximum number of counts for the pulsar is  $20,000 \text{ counts arcmin}^{-2}$ .

brightness emission fills the shell, the emission is concentrated mainly in three prominent components: the pulsar, the jetlike lobe, and the shell. There is a band across the interior to the north of the pulsar of especially low X-ray surface brightness. The count rates from the diffuse emission and from 1E 2259 + 586 are  $8.13 \pm 0.02 \text{ counts s}^{-1}$  and  $1.30 \pm 0.004 \text{ counts s}^{-1}$ , respectively. The average surface brightness of the lobe, shell and interior are 0.023, 0.013, and  $0.009 \text{ counts s}^{-1} \text{ arcmin}^{-2}$ ; that is, the lobe is twice and the interior two-thirds as bright as the shell. Soft X-rays with  $E < 0.5 \text{ keV}$  were detected mainly from the lobe, the northern and southern segments of the shell, and 1E 2259 + 586, as shown in Figure 2. A hard energy map with  $E > 1.5 \text{ keV}$  is similar in appearance to the soft map, indicating that these structures are intrinsically brighter than elsewhere and do not arise from strong column density or temperature variations.

The pulsar is embedded within diffuse emission with a  $2' - 3'$  radius. Figure 3a shows a comparison between the PSPC point-spread function and the profile of the emission from around the pulsar. The profile comparison using the HRI image is shown in Figure 3b. Both profiles show an excess of emission over the point-spread function between  $30''$  and  $3'$ . This extent most likely arises from a compact synchrotron nebula, but a dust scattering halo cannot be ruled out (see § 3.4). In contrast, the radio emission around

the pulsar is elongated in the east-west direction, and no point source is detected (see Fig. 5).

Despite the substantial improvement in sensitivity of the *ROSAT* map over the previous images, there is still no detection of X-ray emission from the shell to the west of the pulsar. If the absence of emission from the west were due to absorption alone, such a long exposure observation might have detected some amount of X-ray emission. Assuming the west has the same spectrum as the rest of the shell, given  $N_H = 2 \times 10^{22} \text{ cm}^{-2}$ , the emission should be detected at the  $2.5 \sigma$  level. For  $N_H > 2.5 \times 10^{22} \text{ cm}^{-2}$  the cloud is capable of absorbing all of the X-ray emission within the PSPC energy band. This is comparable with the  $N_H \sim (2-3) \times 10^{22} \text{ cm}^{-2}$  as measured for the molecular cloud on the west (Tatematsu et al. 1985). While the possibility that the western half of the shell is shadowed in soft X-rays cannot be ruled out using the PSPC data, both the broader band map from the *ASCA* GIS (Corbet et al. 1995) and the radio maps attest to its absence.

We have constructed two hardness ratio maps. The spectral hardness ratio (SHR) map is defined here as the ratio of a high-energy band map to a low-energy band map. Such a map can reveal spectral variations due to absorption and/or temperature. A high value of SHR indicates a locally high column density or temperature. The PSPC SHR map between channels 70–250 ( $\sim 0.7 - 2.2 \text{ keV}$ ) and 30–70 ( $\sim 0.3 -$

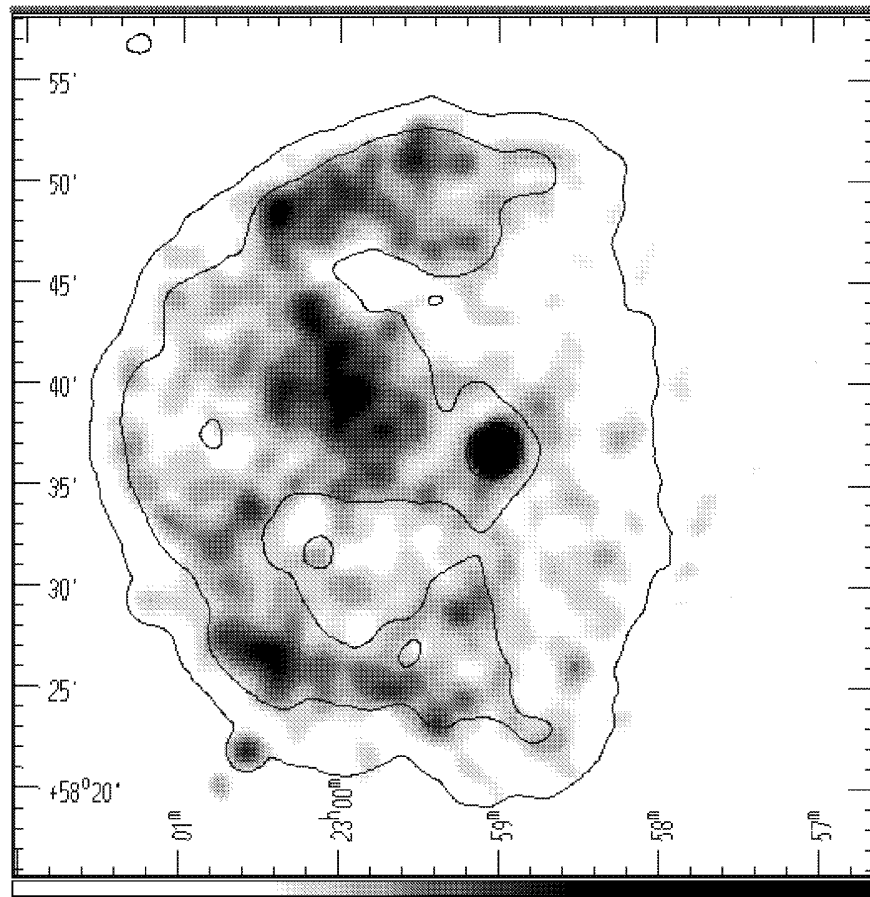


FIG. 2.—The soft band ( $E < 0.5$  keV) PSPC image of CTB 109

0.7 keV) is shown in Figure 4 (*top*); this appears to be the same as the average photon energy map. The SHR is generally higher in the northeast than in the southwest. A second PSPC hardness map (Fig. 4, *bottom*) has been constructed using the ratio between channels 131–250 ( $\sim 1.3$ – $2.2$  keV) and 40–131 ( $\sim 0.3$ – $1.3$  keV). This hardness map shows that the CO ridge extending across the remnant, the eastern shell, and the pulsar are harder than elsewhere, and the jet is softer. This hardness map is approximately anticorrelated with the X-ray intensity map. Based on the spectral fitting (see § 3.3.), we interpret the structure in the first hardness map as primarily resulting from differential absorption, and that in the second hardness map mainly from spectral variations.

### 3.2. Comparison with CO, Radio, and Optical Maps

The high-resolution CO map (Tatematsu et al. 1987) shows that the western boundary of the remnant abuts the edge of the molecular cloud, consistent with the idea that the western portion of the shell is missing as a consequence of the interaction between the two.

In addition, the X-ray emission is slightly enhanced along the western boundary of the remnant, especially between decl.  $58^{\circ}25'$  and  $58^{\circ}35'$  (B1950; see Fig. 5). This is evidence of an interaction between the SNR and the molecular cloud, manifesting itself as higher emission measure from denser material. The “bridge” between the pulsar and southern shell along R.A.  $\sim 22^{\text{h}}59^{\text{m}}20^{\text{s}}$  (B1950) might be a part of this enhanced emission in projection. The CO brightness tem-

perature of the northern arm shows an apparent anticorrelation with the X-ray surface brightness. Tatematsu et al. (1990) have suggested that this anticorrelation is an absorption effect (see § 4.3).

The X-ray and radio images show the same general shell structure, but the surface brightness peaks along the shell are at different locations, as shown in Figure 5, an overlay of the PSPC image on a 20 cm radio continuum map with  $1'$  resolution (Gregory et al. 1983). While the shell has the same overall shape in the two bands, the interior shows very different morphologies. In particular, the pulsar and the lobe are invisible in the radio. A radio point source is located about  $2'$  away from 1E 2259+586, but no association with the pulsar is known (Hughes et al. 1984). The fact that X-ray and radio images both show a semicircular shape supports the idea the shell is truly missing rather than hidden by the cloud.

A correlation between the optical filaments and the brightest parts of the radio shell in the northeast and south (Hughes, Harten, & van den Bergh 1981) indicates that both are related to the shock compression of ambient material. Interestingly, an optical filament has been found along the southwestern edge of the X-ray lobe (Fesen & Hurford 1995). The emission mechanism for this filament might be different from that of the shell, although a projection effect cannot be ruled out. While one might expect optical emission along the boundary of the interaction between the SNR and a large cloud because of radiative cooling, if the cloud density is high such as in a molecular cloud, then it is

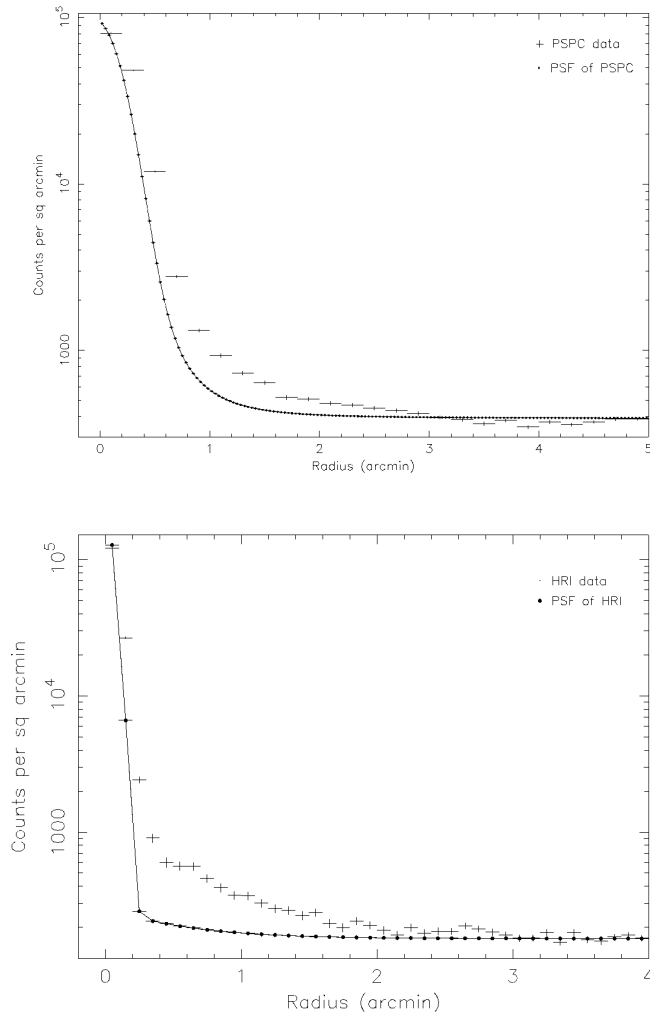


FIG. 3.—The radial profiles of the pulsar and point-spread function (solid line) are plotted for PSPC and HRI. The PSPC radial profile is compared with the PSPC point-spread function in (a) and HRI data and point-spread function in (b).

likely that the dense cloud has decelerated the shock sufficiently that the bulk of the radiation is emitted in the IR band.

### 3.3. Spectral Observations of CTB 109

Using the PSPC spectral capability in conjunction with the BBXRT data, we can characterize the general spectral properties of the diffuse emission in CTB 109 and search for spectral variations across the remnant. Our approach here is first to use a combination of BBXRT and PSPC data to perform detailed spectroscopy of the region observed by the BBXRT and then to carry out spectral mapping of the entire remnant using the PSPC data. For the BBXRT/PSPC analysis, our starting point is the time-dependent equilibrium models of Hamilton, Sarazin, & Chevalier (1983, HSC hereafter). These models offer an opportunity to obtain a realistic view of the physical conditions, and the relative metal abundances, at least in a portion of the remnant. As the PSPC offers restricted spectral capability, and the data allow at best a discrimination between a single temperature and a multitemperature model, we use for our spectral mapping coronal equilibrium ionization models (Raymond & Smith 1977). While limiting our ability to

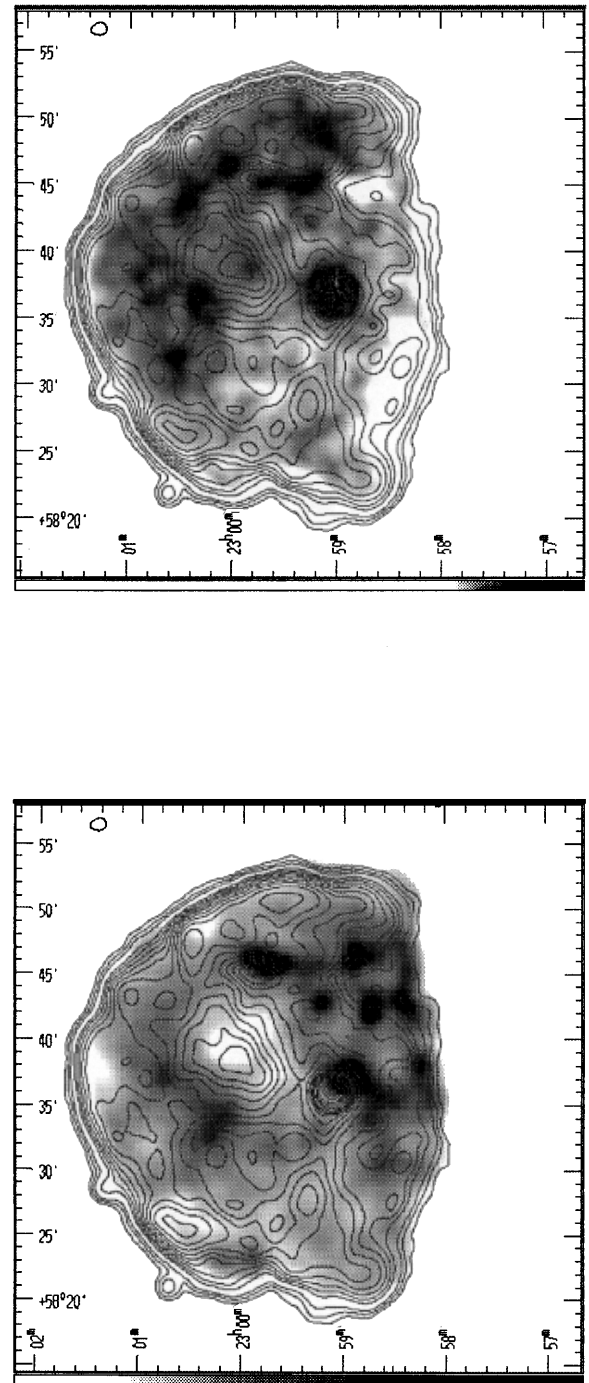


FIG. 4.—*Top*: The PSPC (0.7–2.2 keV/0.1–0.7 keV) spectral hardness ratio (SHR) map in gray scale, superposed on PSPC contours. Darkness corresponds to increasing spectral hardness. The darkest regions have SHR 4–7, and the faint gray regions have SHR  $\sim 1$ . This SHR map is virtually identical to the average photon energy map. *Bottom*: The 1.3–2.2 keV/0.1–1.3 keV SHR map, superposed on PSPC contours. The lobe (faint gray) has SHR  $\sim 0.01$ –0.2, while the rest of the remnant (dark gray) has SHR  $\sim 0.55$ –0.8.

draw conclusions about the details of the physical conditions, this approach does allow us to search sensitively for spectral variations.

In Figure 6a, we overlay the BBXRT field of view on the PSPC image. Only the interior of the remnant south and southeast of the pulsar has been observed; the lobe was

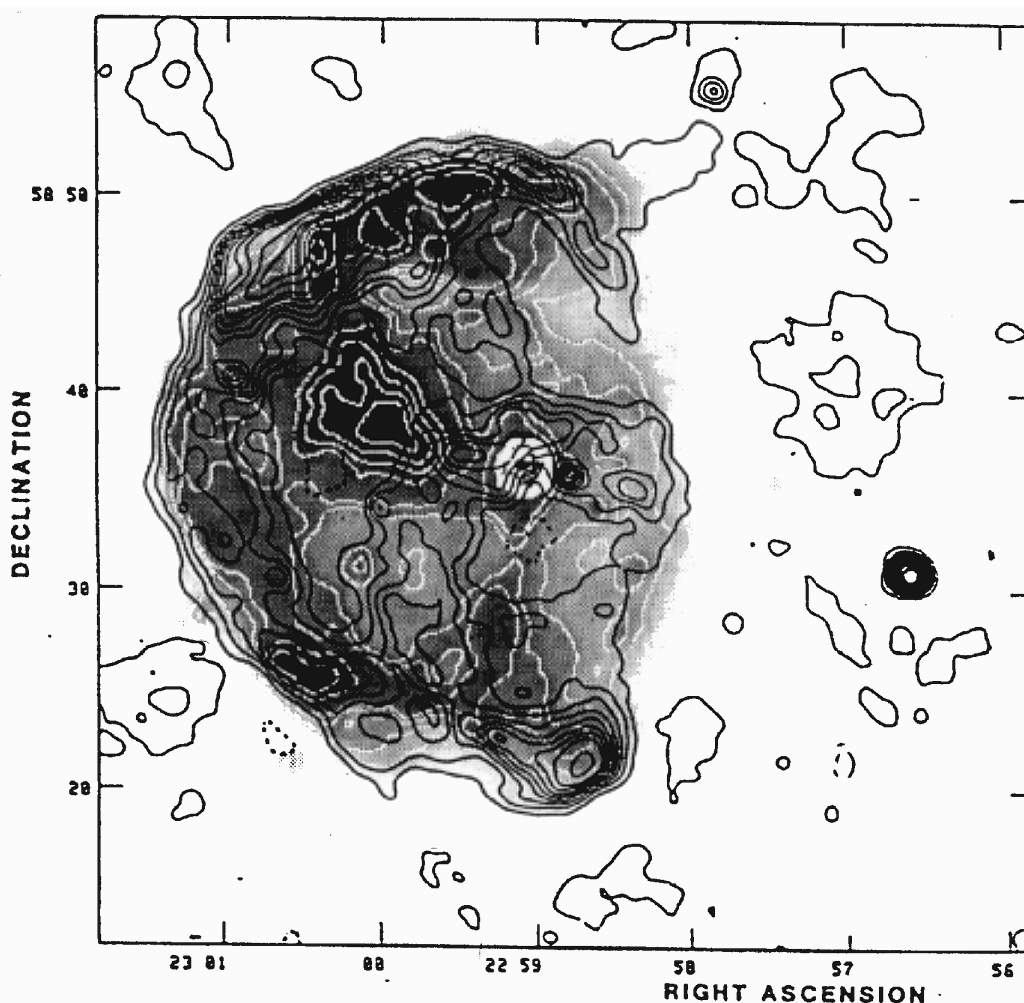


FIG. 5.—The X-ray map and contours (white lines) are superposed on radio contours (black lines) from Gregory et al. (1983)

entirely missed by the BBXRT. We used only the data from the detector element pairs A3/B1 and A4/B2, as they were the only ones with sufficient signal-to-noise ratios to allow meaningful spectral fitting. The raw BBXRT spectra are shown in Figure 6b. The detector element that collected each spectrum is indicated in the figure. We have simultaneously fitted all four of these spectra, plus the spectrum of the PSPC data extracted from the region viewed by the BBXRT. These data have been fitted using the HSC models for both the instantaneous electron-ion equipartition case ( $T_e = T_i$ ) and the case for which equipartition occurs in a time-dependent way via Coulomb collisions ( $T_e \neq T_i$ ). The grid of models and the limitations on their use have been explained in Rho et al. (1994).

The best-fit results for the two cases are listed in Table 1, along with the inferred metal abundances. Included, for reference, is the best-fit two-temperature coronal equilibrium plasma model. The best-fit model for the nonequipartition case is shown superposed on the A3/B1 spectra in Figure 7a. Equally good fits are obtained using the two sets of models. They yield qualitatively different results, however: equipartition requires an approach to ionization equilibrium ( $T_s = 1.8 \times 10^6$  K;  $\eta = 10^{51}$  ergs cm $^{-6}$ ;  $n_0 t \sim 17,000$  cm $^{-3}$  yr), and nonequipartition requires extreme nonequilibrium conditions ( $T_s = 2 \times 10^7$  K;  $\eta = 10^{49}$  ergs cm $^{-6}$ ;  $nt = 430$  cm $^{-3}$  yr). These differences can be understood in the following way. The ratio of the Ne ix He $\alpha$  line

at approximately 915 eV to Ne x Ly $\alpha$  at about 1.00 keV is large ( $8 \pm 2.5$ ), requiring either a low shock temperature or a low  $n_0 t$  product. At the same time, the slope of the continuum above about 2 keV is relatively flat, with  $-d \ln(\text{energy flux})/d \ln(\text{photon energy}) = 6.1 \pm 1.8$ . The flat slope indicates a high shock temperature, and while the equipartition models are generally less sensitive to the shock temperature, most of parameter space is ruled out. The allowed 90% confidence ranges in  $T_s$ - $\eta$  parameter space for  $T_i \neq T_e$  and  $T_i = T_e$  are shown in Figure 7b. These represent the regions of parameter space that are allowed mutually by the continuum spectral index and the Ne ix/Ne x ratio. For the nonequipartition models, which are more sensitive to the continuum slope, a high shock temperature is required, which in combination with the high Ne ratio forces a solution with a high shock temperature and a low ionization age.

The current data offer no means of resolving whether the plasma is in equipartition. The equipartition model is slightly preferred (the reduced  $\chi^2$  is lower), and the shock temperature is consistent with the electron temperature obtained when fitting equilibrium models to the PSPC data. On the other hand, there are ample physical reasons for expecting electron-ion equipartition to occur slowly or not at all in SNR shocks (Shklovsky 1968). Additionally, the abundances for the nonequipartition fit are consistent with solar, which is more plausible for a  $10^4$  yr old SNR presum-

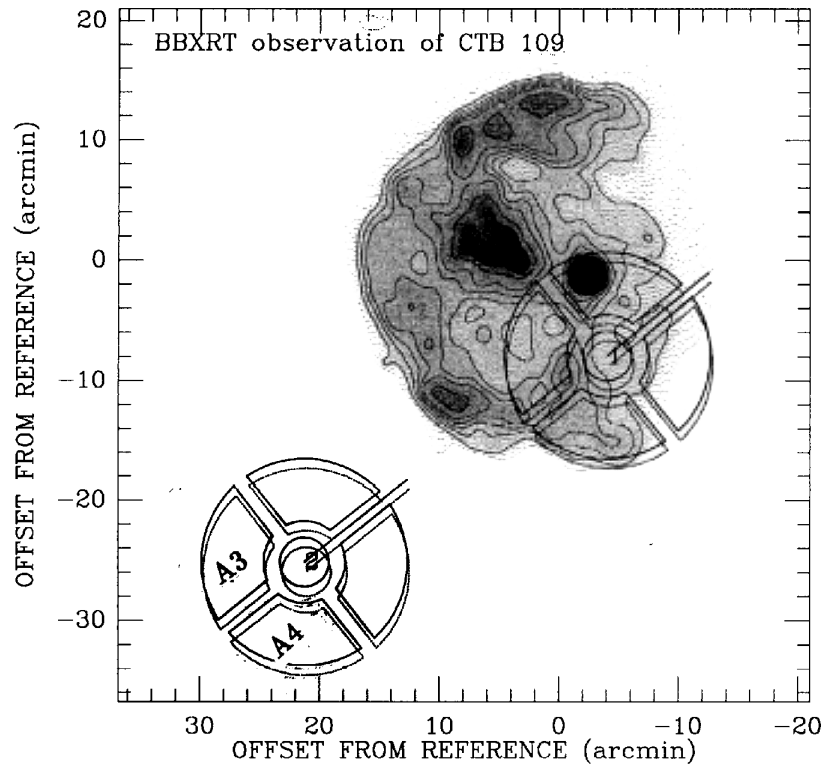


FIG. 6a

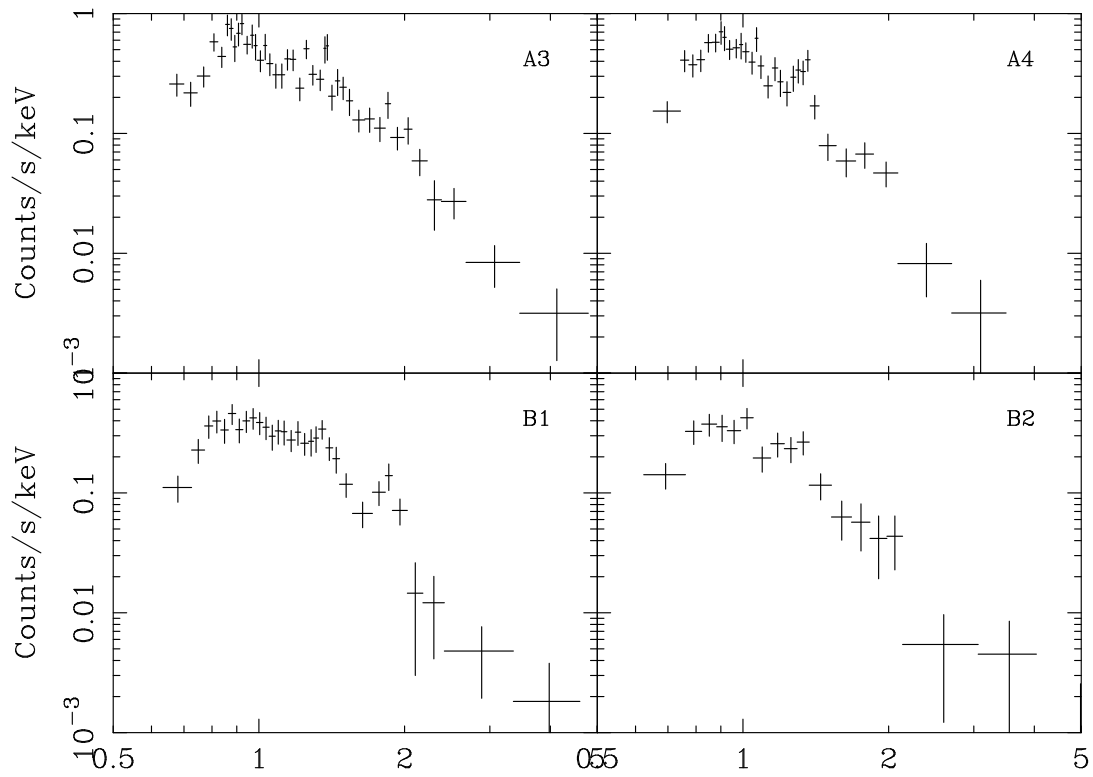


FIG. 6b

FIG. 6.—(a) The field of view of BBXRT data superposed on the PSPC image; the detector elements are indicated. (b) The BBXRT spectra.

TABLE 1  
BBXRT/PSPC SPECTRAL FITS

Data	BBXRT <sup>a</sup>	BBXRT+PSPC ( $T_i \neq T_e$ )	BBXRT+PSPC ( $T_i = T_e$ )
Model .....	2T equilibrium <sup>b</sup>	NEI	NEI
$\chi^2/\nu^c$ .....	2672/1032 $\sim$ 2.5	700/652 $\sim$ 1.0	688/652 $\sim$ 1.0
$T$ .....	$kT_{\text{low}} = 0.26$ keV	$T_s = 10^{7.25}$ K	$T_s = 10^{6.25}$ K
$T$ .....	$kT_{\text{high}} = 2.7$ keV	$\eta = 10^{4.9d}$	$\eta = 10^{5.1}$
$T$ .....	...	$n_0 t = 430^d$	$n_0 t = 17,000$
$N_H(10^{21} \text{ cm}^{-2})$ .....	$6.4^{+1.4}_{-1.8}$	$9.0 \pm 0.8$	$7.2 \pm 0.5$
O <sup>e</sup> .....	$0.0^{+0.09}_{-0.1}$	1.0 (fixed)	1.0 (fixed)
Ne .....	$0.17^{+0.11}_{-0.06}$	$0.6^{+0.4}_{-0.3}$	$1.7^{+0.9}_{-0.7}$
Mg .....	$0.28^{+0.14}_{-0.11}$	$1.1^{+0.6}_{-0.4}$	$5.0^{+3.3}_{-2.0}$
Si .....	$0.65^{+1.95}_{-0.24}$	$1.7^{+1.2}_{-0.8}$	$6.1^{+3.7}_{-2.0}$
S .....	...	$1.5^{+3.4}_{-1.5}$	$8.6^{+10.5}_{-7.9}$
Fe .....	$0.06^{+0.40}_{-0.03}$	$2.0^{+1.1}_{-0.7}$	$2.8^{+1.3}_{-0.6}$

<sup>a</sup> Pulse-height channels 40–300 ( $\sim 0.6$ – $6.0$  keV) were used for the BBXRT spectra.

<sup>b</sup> Two-temperature equilibrium.

<sup>c</sup>  $\nu$  is number of degrees of freedom.

<sup>d</sup>  $\eta$  and  $n_0 t$  have units of  $\text{ergs cm}^{-6}$  and  $\text{cm}^{-3} \text{ yr}$ , respectively.

<sup>e</sup> All abundance units are relative to solar values.

ably dominated by swept-up interstellar medium (ISM) material than the 2–3 times solar abundances of the equipartition case. One possible explanation preserving non-equipartition is that we are observing a superposition of two NEI components. The current data are of inadequate quality to test this hypothesis, and the addition of a second NEI component does not improve the fit significantly.

To investigate whether the conditions in the region observed by the BBXRT are typical of the remnant as a whole, we divided the PSPC image into a number of regions, based on morphology, and fitted the spectrum of each (Fig. 8, *bottom*). Fits using a power law, and a one- and two-temperature Raymond-Smith coronal plasma model were carried out. While acceptable fits were obtainable using NEI models, the larger number of free parameters led to large error ranges, and consequently an inability to distinguish spectral differences from one region to another. The results for the best-fit models are summarized in Table 2: temperatures and column densities obtained for acceptable collisional ionization equilibrium models, along with the reduced  $\chi^2$ . Metal abundances were varied jointly for the low- and high-temperature components unless otherwise specified. The regions can be divided into three groups based on the best-fit models. A single-temperature model gave acceptable fits for the interior region and the eastern shell (regions “D,” “F,” and “C”), but a two-temperature model is required for the lobe and the northern and southern shell segments (regions “B,” “A,” and “G”). A power law, a blackbody, and bremsstrahlung all provide acceptable fits for the PSPC spectrum of the pulsar. We have therefore included *ASCA* and BBXRT spectra for further analysis (§ 3.4).

The spectrum of the lobe is thermal. The fit to a power-law model is unacceptable, as shown in Table 2, indicating that there is no evidence for synchrotron or other non-thermal radiation. An acceptable fit is obtained using a two-temperature thermal model in which Mg, Si, and S are varied together with  $kT_{\text{low}} = 0.16^{+0.03}_{-0.04}$  keV,  $kT_{\text{high}} = 0.56^{+0.2}_{-0.1}$  keV, and  $N_H = 0.92^{+0.10}_{-0.15} \times 10^{22} \text{ cm}^{-2}$ . There is no evidence of enhanced metal abundances, indicating the structure is not related to supernova ejecta; the abundances

of Mg, Si, and S (0.1–0.6 solar) are similar to those obtained in the fit to the BBXRT spectra (Table 1).

The spectra of the interior (regions “D” and “F”) and the eastern shell (region “C”) are adequately fitted by a single-temperature model. These fits are all formally acceptable at the 90% confidence level ( $\chi^2_\nu < 1.46$  for 17 degrees of freedom; see Bevington & Robinson 1969). The two-temperature model yielded acceptable fits and similar temperatures to those of the lobe, but the improvement in  $\chi^2$  was negligible. The temperature for the single-component model varies slightly across the remnant with values between  $0.18 \pm 0.05$  keV and  $0.30 \pm 0.05$  keV. The temperature obtained for the southern interior, coincident with the BBXRT pointing, is consistent with both the lower temperature obtained from the two-component fit to the BBXRT and PSPC data (the emission from the higher temperature material is largely above the PSPC band) and, more importantly, the shock temperature from the equipartition HSC model.

In contrast, the northern and southern shell segments require a second component. The temperatures, metal abundances, and  $N_H$  values are virtually identical to those of the lobe. For the southern shell, obtaining an acceptable fit required a subsolar Ne abundance as well. Taken together, the PSPC fit results suggest that the ionization conditions vary across the SNR: some regions (those requiring two components) are further from ionization equilibrium than others. A more careful examination of the ionization conditions across the remnant awaits higher resolution X-ray spectroscopic observations. An example of PSPC spectra, from the segment of the shell and the interior, is shown in Figure 8 (*top*), respectively.

The column density gradually decreases by about 20% from the northeast to the southwest with a range  $8.0$ – $10.2 \times 10^{21} \text{ cm}^{-2}$ , largely consistent with the low-energy (0.7 keV) cut hardness map, as shown in Table 2 and Figure 8 (*bottom*). The hardness map also suggests the presence of column density variation on smaller scales, but these variations are not quantifiable using the current data. The extinction toward CTB 109 is  $E(B - V) = 1.1$ , estimated from two Sharpless H II regions (Sharpless 1959). The



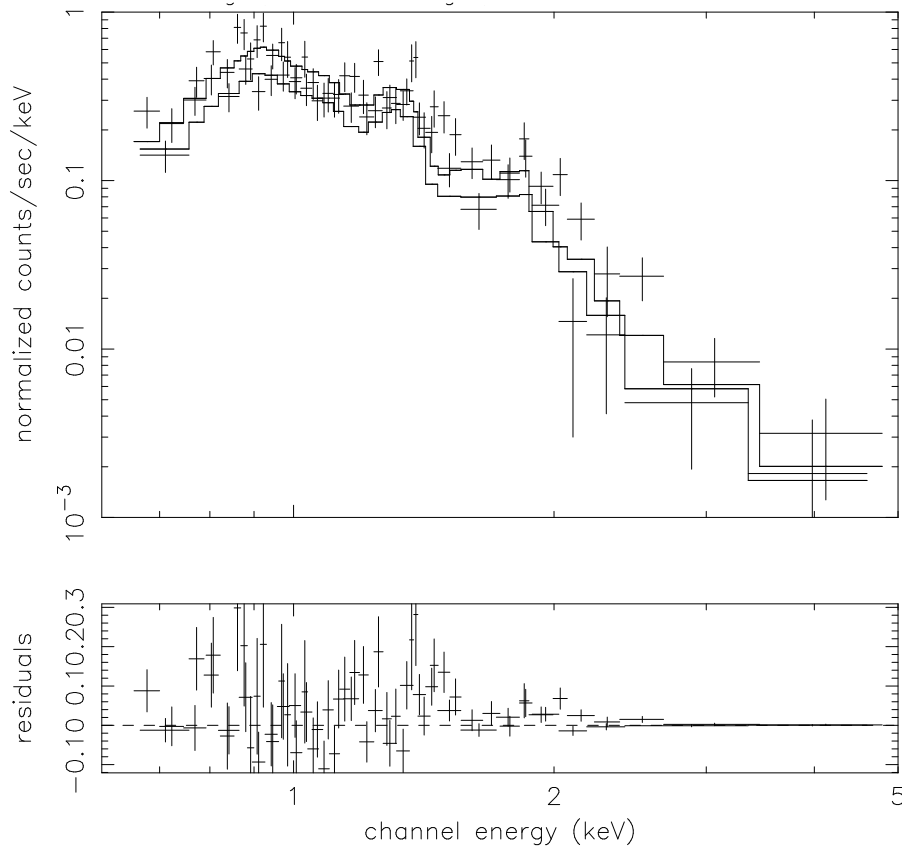


FIG. 7a

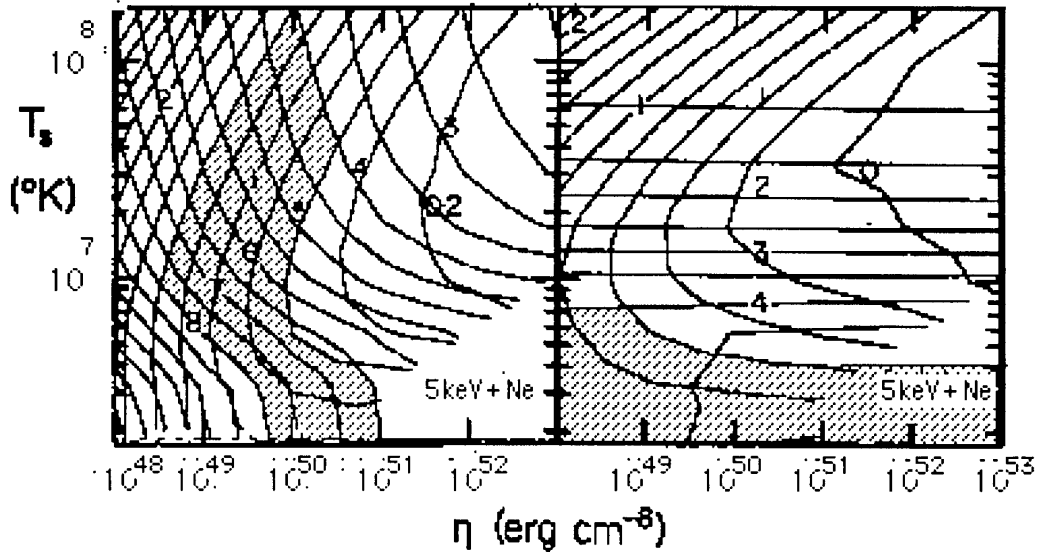


FIG. 7b

FIG. 7.—(a) The best-fit nonequilibrium model superposed on spectra from BBXRT elements A3/B1. (b) Allowed 90% confidence ranges (*dashed lines*) of the shock temperature and ionization parameter  $\eta$  (x-axis with units of  $\text{cm}^{-6} \text{ yr}$ ) from the continuum spectral index (at 5 keV) and the ratio of Ne IX/Ne X for (*left*) nonequipartition  $T_i \neq T_e$  and (*right*) equipartition  $T_i = T_e$  cases. This figure is a reproduction of Figs. 3 and 9 of HSC to demonstrate the allowed ranges of  $T_s$  and  $\eta$ .

optical spectrum of the remnant could not be used to estimate  $E(B-V)$  because  $H\beta$  was not detected (Blair & Kirshner 1981). The relationship between  $N_H$  and extinction,  $N_H/E(B-V) = (6.8 \pm 1.6) \times 10^{21} \text{ H atoms cm}^{-2} \text{ mag}^{-1}$  (Gorenstein & Tucker 1976) predicts  $N_H = 7.5 \pm 1.8 \times 10^{21} \text{ cm}^{-2}$ . This value is consistent with the  $N_H$  obtained by spectral fitting, as shown in Table 2. The CO arm region

has no higher  $N_H$  value than the nearby lobe, even though the CO arm itself is expected to contribute additional  $N_H$ .

A composite spectrum of the diffuse emission, i.e., the entire remnant excluding the pulsar, has been fitted using one- and two-temperature models as listed in Table 3. The two-temperature model fit is preferred over the one-temperature model and gives temperatures of  $0.17 \pm 0.02$

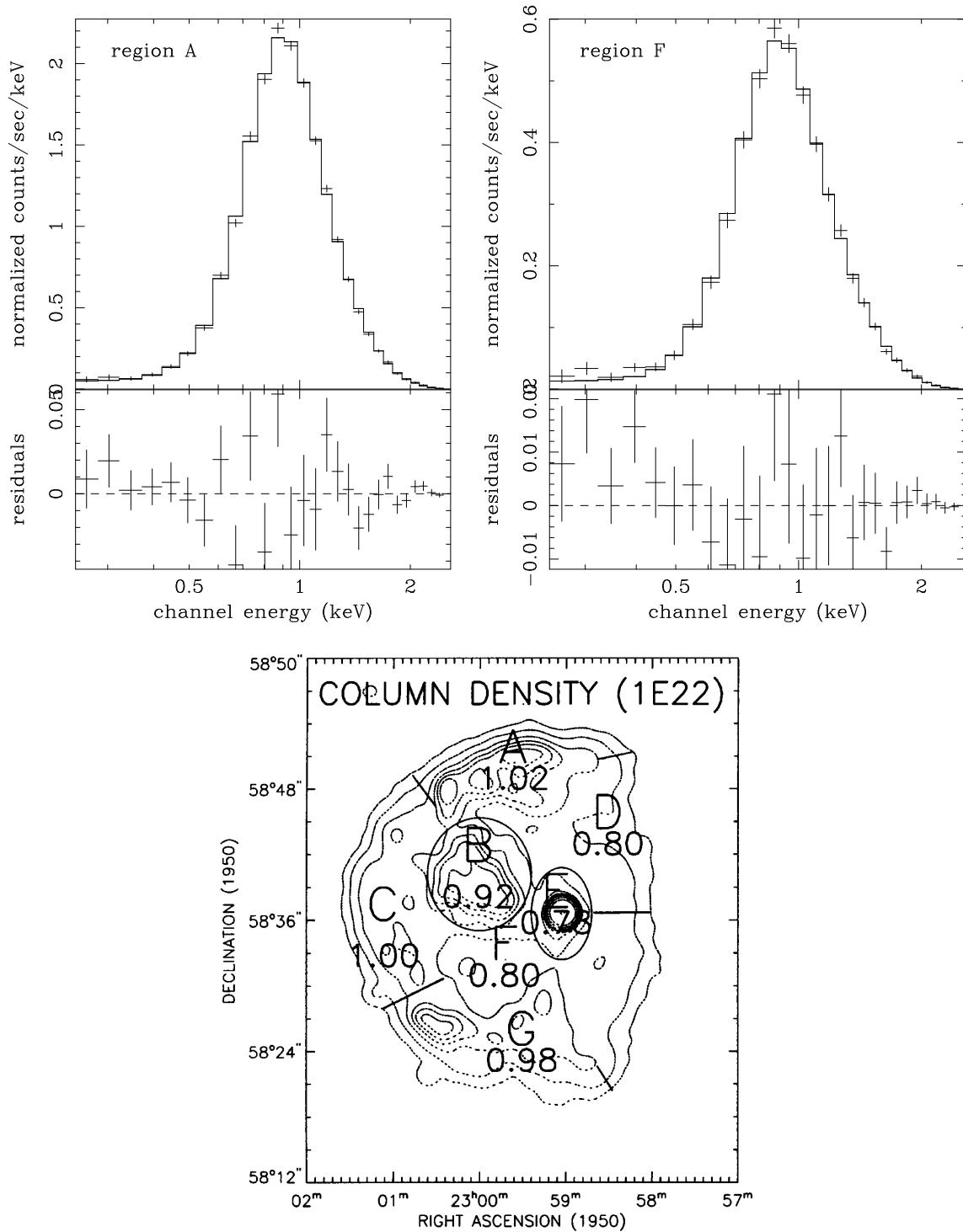


FIG. 8.—The PSPP spectra of (top left) the northern shell (region “A”) and (top right) southern interior (region “F”) and the best fits. The fit residuals are also shown. The absorption distribution is shown on X-ray contours (bottom). Units are  $10^{22} \text{ cm}^{-2}$ , and the typical 90% confidence range is  $\pm 0.1 \times 10^{22} \text{ cm}^{-2}$ .

keV and  $0.56 \pm 0.15 \text{ keV}$ . The inferred physical parameters of the SNR using the parameters from the two-temperature model are listed in Table 3.

### 3.4. The Pulsar and Surrounding Emission

The anomaly of 1E 2259+586 is that its rotational energy-loss rate is only  $10^{32} \text{ ergs s}^{-1}$ , 3 orders of magnitude less than its X-ray luminosity. It is neither a high-mass X-ray binary nor a rotationally powered neutron star like

the Crab pulsar. No direct evidence has been found to show it is a member of a binary system. The fact that its spin-down rate has decreased by a factor of 2 has ruled out an isolated white dwarf model, since that model requires an extremely stable  $\dot{P}$  (Iwasawa et al. 1992).

We simultaneously fitted *ASCA* (GIS2 and SIS0), *BBXRT*, and PSPP spectra to obtain the best model for 1E 2259+586. The *ASCA* data were extracted from the archive; results of fitting the *ASCA* and *BBXRT* spectra have been reported by Corbet et al. (1995). While the *ASCA*

TABLE 2  
SPECTRAL FIT RESULTS FOR EACH REGION OF CTB 109

Mark (Fig. 8, bottom)	Region (Model) <sup>a</sup>	$\chi^2/\nu$	$N_H^b$ ( $10^{22} \text{ cm}^{-2}$ )	$kT_{\text{low}}^b$ (keV)	$kT_{\text{high}}^b$ (keV)
A .....	Northern shell (2T [Mg])	23/16 ~ 1.4	$1.02 \pm 0.06$	$0.17^{+0.07}_{-0.05}$	$0.56^{+0.35}_{-0.2}$
B .....	Jetlike lobe (2T [Mg])	20/16 ~ 1.26	$0.92^{+0.10}_{-0.15}$	$0.16^{+0.03}_{-0.04}$	$0.56^{+0.2}_{-0.1}$
	Jetlike lobe (power)	1060/24 ~ 42.0	1.4	$\Gamma = 10$	...
G .....	Southern shell (2T [Mg])	17/16 ~ 1.14	$0.98 \pm 0.05$	$0.16 \pm 0.04$	$0.56 \pm 0.04$
C .....	Eastern shell (1T)	20.6/17 ~ 1.2	$1.00 \pm 0.10$	$0.21^{+0.05}_{-0.04}$	...
D .....	CO ridge (1T)	33/25 ~ 1.3	$0.80^{+0.12}_{-0.15}$	$0.30^{+0.07}_{-0.03}$	...
D .....	CO peak (1T) <sup>c</sup>	27/25 ~ 1.1	$1.1 \pm 0.1$	$0.18 \pm 0.05$	...
F .....	Southern interior (1T)	22/25 ~ 0.9	$0.80 \pm 0.15$	$0.29 \pm 0.06$	...
E .....	Pulsar sum (power [1'96]) <sup>d</sup>	26.6/19 ~ 1.40	$0.78 \pm 0.05$	$\Gamma = 3.0 \pm 0.3$	...
E .....	Pulsar sum (BB [1'96])	25.6/19 ~ 1.35	$0.43 \pm 0.04$	$0.36 \pm 0.03$	...
E .....	Pulsar sum (brem [1'96])	25.3.6/19 ~ 1.33	$0.64 \pm 0.04$	$1.1^{+0.20}_{-0.13}$	...
E .....	Pulsar (power [0'5])	31.2/21 ~ 1.46	$1.14 \pm 0.08$	$\Gamma = 4.1 \pm 0.3$	...
E .....	Diffuse nebula (power + 1T) <sup>e</sup>	17.2/17 ~ 1.0	$0.84 \pm 0.3$	$\Gamma = 3.5^{+0.8}_{-1.8}$	$0.22^{+0.16}_{-0.05}$
Using BBXRT, PSPC, and ASCA (GIS2 and SIS0) Data					
E .....	Pulsar (power + BB)	1207/1316 ~ 0.92	$0.85 \pm 0.04$	$\Gamma = 4.0 \pm 0.1$	$kT = 0.43 \pm 0.02$
E .....	Pulsar (power + brem)	1303/1316 ~ 0.99	$0.8^{+0.6}_{-0.1}$	$\Gamma = 4.0^{+0}_{-0.2}$	$kT = 1.04^{+0.08}_{-0.16}$
E .....	Pulsar (power + edge)	1848/1320 ~ 1.4	$1.19 \pm 0.02$	$\Gamma = 4.4 \pm 0.1$	$E = 1 \text{ keV } (\tau = 0.7)$

<sup>a</sup> 1T and 2T indicate one- and two-temperature thermal models. The terms “power,” “BB,” and “brem” indicate power law, blackbody, and bremsstrahlung model, respectively.  $\Gamma$  is the photon index of the power law. [Mg] indicates the abundance of Mg, Si, and S (also Ne for region G) varied together. The edge model is a cyclotron absorption line at the energy of 1 keV.

<sup>b</sup> All errors represent 90% confidence regions. Unacceptable fits are listed without errors for comparison.

<sup>c</sup> CO peak region is where the X-ray surface brightness is anticorrelated to CO intensity.

<sup>d</sup> The number in brackets indicates the radius of the region from which the spectrum was extracted.

<sup>e</sup> The spectrum of the diffuse nebula is extracted from the elliptical annulus  $[(2.5 \times 3.5) \text{ to } (1.9 \times 1.9)]$ .

data offer moderate spectral resolution and cover a higher energy band, the PSPC spectrum provides coverage of the 0.1–1 keV band, which is important for constraining  $N_H$  and other parameters. Single-component models, power law ( $\chi^2_\nu \sim 2.1$ , where  $\nu = 1320$ ), bremsstrahlung ( $\chi^2_\nu \sim 1.28$ ), and blackbody ( $\chi^2_\nu \sim 1.73$ ), are formally rejected. Models combining a power law plus a blackbody, and a power law plus bremsstrahlung, yield acceptable fits; the results are summarized in Table 2. The power-law/blackbody parameters are largely consistent with those of Corbet et al. (1995),

with  $\Gamma = 4.0 \pm 0.1$  and  $kT = 0.43 \pm 0.02$  keV. However, Corbet et al. (1995) found a lower  $N_H$  value ( $4.3 \times 10^{21} \text{ cm}^{-2}$  using GIS spectra), while all of our fits yielded  $N_H \sim 8.5 \times 10^{21} \text{ cm}^{-2}$ . Our value is more consistent with that in other regions of the remnant and the extinction value in this direction. Addition of a cyclotron absorption line to the power-law model did not yield an acceptable fit. A search for absorption features is motivated by the marginal detection at a cyclotron line at about 7 keV by Ginga (Koyama et al. 1989).

TABLE 3  
FIT RESULTS OF DIFFUSE EMISSION OF CTB 109 FROM TWO-COMPONENT  
THERMAL MODEL

Parameter	Value
$\theta$ (arcmin) .....	$28' \times 34'$
Distance (kpc) .....	4 ( $1' = 1.164 \text{ pc}$ )
$d$ (diameter [pc]) .....	$32.6 \times 39.6$ ( $r = 19 \text{ pc}$ )
Count rate (counts $\text{s}^{-1}$ ) .....	8.13
$\chi^2/\nu$ .....	34/25 ~ 1.36
$N_H$ ( $10^{21} \text{ cm}^{-2}$ ) .....	$10.2 \pm 0.3$
$kT_{\text{low}}$ (keV) .....	$0.17 \pm 0.02$
$kT_{\text{high}}$ (keV) .....	$0.56 \pm 0.15$
Flux (ergs $\text{s}^{-1} \text{ cm}^{-2}$ [0.2–2.4 keV]) .....	$7.8 \times 10^{-11}$
Unabsorbed flux <sup>a</sup> .....	$1.8 \times 10^{-8}$
$L_X$ (ergs $\text{s}^{-1}$ ) .....	$3.2 \times 10^{37}$
Normalization $k_{\text{low}} [k_{\text{high}}]^b$ .....	$2.9^{+4.3}_{-0.3} [0.05^{+0.10}_{-0.01}]$
$n_{\text{e[low]}}$ assuming 20% shell $[n_{\text{e[high]}}]$ ( $\text{cm}^{-3}$ ) .....	$1.2^{+0.6}_{-0.2} [0.11^{+0.09}_{-0.02} f^{-1/2}]^c$
$m_{\text{X[low]}} [m_{\text{X[high]}}]$ ( $M_\odot$ ) .....	440 [50]
Shock velocity $= v_s$ ( $\text{km s}^{-1}$ ) .....	380
Age (yr) .....	$1.9 \times 10^4$
Energy (ergs) .....	$1.0 \times 10^{51}$

<sup>a</sup> Unabsorbed flux in the 0.2–2.4 keV band.

<sup>b</sup> Normalization has units of  $10^{-14} n_e^2 V / 4\pi d^2$  ( $\text{cm}^{-3}$ ).

<sup>c</sup> The term  $f$  is the filling factor of the hot component.

The power-law/bremsstrahlung model also yielded an acceptable fit with  $\Gamma = 4^{+0.2}_{-0.2}$ ,  $kT = 1.04^{+0.08}_{-0.16}$  keV. Corbet et al. (1995) also found an acceptable fit to the *ASCA* GIS spectra using this model, but with an unrealistically flat spectral index ( $\Gamma \sim 0$ ). For our fit, the large emission measure ( $n^2V \sim 3.8 \times 10^{58} \text{ cm}^{-3}$ ) of the bremsstrahlung component would require the radius of the emitting gas region to be many orders of magnitude larger than for a neutron star. Similar fit results have been reported for 4U 0142+61 (White et al. 1996). While this model could in principle indicate a neutron star surrounded by plasma in an extended halo, the required 2–3 pc radius of such a halo could not be gravitationally bound to the neutron star.

The PSPC spectrum extracted from within an approximately  $2'$  radius of 1E 2259 + 586 is well fitted within 99% confidence by either a power law, a bremsstrahlung model, or a blackbody. The power-law indices within  $30''$  and  $2'$  of the pulsar are  $\Gamma = 4.1 \pm 0.3$ , and  $3.0 \pm 0.3$ , respectively, indicating that the spectrum including the halo emission becomes harder. This suggests that the halo does not arise from dust scattering: the energy dependence of the dust scattering cross section ( $E^{-2}$ ) would produce a larger photon index with increasing distance from the pulsar. We confirm this result by fitting two power-law models to the pulsar spectrum (within  $2'$ ): after we fixed the first power-law component to  $\Gamma = 4$  and  $N_H = 8.5 \times 10^{21} \text{ cm}^{-2}$ , we found  $\Gamma = 2.5 \pm 1.0$  for the second component. While the broadening of the PSPC point spread-function with increasing energy above 1 keV could in principle produce an apparent hardening of the halo with increasing radius, this effect is small compared with the spectral hardening observed, given the steep source spectrum.

Neither does the extent of the emission favor the scattering halo hypothesis. Figure 3 shows that the extended flux is 20%–30% that of the point source, which is much larger than the typical scattering halo fraction (12%) for  $N_H = 8.5 \times 10^{21} \text{ cm}^{-2}$  ( $A_v \sim 3.3$ ), assuming a uniform ISM along the line of sight (Predehl & Schmitt 1995). On the other hand, since the fractional intensity of a dust-scattered X-ray halo depends on numerous free parameters, including the physical properties of the grains and their spatial distribution, it is hard to rule out the possibility that we are observing a halo. The contribution by grains to the halo surface brightness is inversely proportional to the scattering angle and directly proportional to the grain size (Mathis & Lee 1991). The full width at half-maximum of the scattered light is about  $2\pi a/\lambda$ , where  $a$  is the grain size and  $\lambda$  is the wavelength of the incident radiation. If the extended emis-

sion is due to scattering, then the dust particles must be concentrated around the pulsar, considering that the halo fraction is larger than for a uniform medium.

The diffuse emission around the pulsar, in a region confined by an outer ellipse of major and minor axes  $3.5$  and  $2.5$  and an inner circle of diameter  $1.9$  (elliptical annulus region:  $2.5 \times 3.5$  to  $1.9 \times 1.9$ ) contains both thermal and non-thermal spectral components. The thermal emission with  $kT = 0.22^{+0.16}_{-0.05}$  keV contributes a slightly larger (60%) fraction of the total flux than the nonthermal emission with  $\Gamma = 3.5^{+0.8}_{-1.8}$  (see Table 2). An effort to separate the thermal and nonthermal components spatially by extracting smaller and different elliptical regions was unsuccessful.

The best-fit pulsar spectrum yields an absorbed 0.5–10.0 keV flux of  $2.7 \times 10^{-11} \text{ ergs s}^{-1} \text{ cm}^{-2}$ , an unabsorbed flux of  $1.75 \times 10^{-10} \text{ ergs s}^{-1} \text{ cm}^{-2}$ , and an X-ray luminosity of  $3.0 \times 10^{35} \text{ ergs s}^{-1}$ . The X-ray luminosity is comparable to that of the pulsar in MSH 15–52 (Seward & Harnden 1982), 2 orders of magnitude higher than that of PSR 151+32 in CTB 80 (Safi-harb, Ogelman, & Finley 1995) and the Vela pulsar (Harnden, Grant, & Seward 1985), and only 10% of that of Crab pulsar.

The pulsar period has been obtained by period folding around the peak frequency of the fast Fourier transform of the barycenter-corrected PSPC event arrival times. The period so obtained is  $6.978814 \pm 9.4 \times 10^{-6} \text{ s}$ . The inferred  $\dot{P}$  value using the PSPC and *Ginga* periods is  $4.369 \times 10^{-13} \text{ s s}^{-1}$ , and using the PSPC and *Einstein* IPC is  $5.880 \times 10^{-13} \text{ s s}^{-1}$ . The pulse period history is shown in Koyama et al. (1989). The PSPC period is consistent with a constant  $\dot{P}$ , which agrees with that from the *ASCA* observation (Corbet et al. 1995). The PSPC pulsed profile is shown as a folded light curve in Figure 9.

### 3.5. Other Point Sources in the Field of View

In addition to the pulsar 1E 2259 + 586, six point sources are detected in the field of view. These are listed in Table 4. None of them has any cataloged counterpart at other wavelengths. Two of them are a few arcminutes to the west of the pulsar, which are inside the remnant in projection. Two others are located outside the edge of the southeastern shell. The fifth source is located at the west of the remnant and would also be inside the remnant in projection, if the remnant were circular. The results of spectral fitting using a Raymond-Smith thermal model are also listed in Table 4. Fits could not be performed on the spectra of sources 5 and 6 because of the lack of counts. For spectral fitting of the sources inside the remnant (point sources 1 and 2), the SNR

TABLE 4  
POINT SOURCES DETECTED IN FIELD OF VIEW

Source	R.A. (1950)	Decl. (1950)	COUNTS	SPECTRAL FITTING	
				$N_H (10^{22} \text{ cm}^{-2})$	$kT \text{ (keV)}$
1 .....	22 58 27.8	58 36 53.1	440	$1.3^{+0.3}_{-0.5}$	$0.17 \pm 0.07$
2 .....	22 58 37.4	58 34 38.1	480	$1.1 \pm 0.4$	$0.20 \pm 0.15$
3 .....	23 01 16.2	58 29 17.2	510	$1.0 \pm 0.4$	$0.13 \pm 0.05$
4 .....	23 00 35.6	58 21 49.8	240	$1.5 \times 10^{-2}$	0.27
5 <sup>a</sup> .....	22 57 28.3	58 36 06.9	100	...	...
6 <sup>a</sup> .....	23 01 18.3	58 57 02.0	180	...	...

NOTE.—Units of right ascension are hours, minutes, and seconds, and units of declination are degrees, arcminutes, and arcseconds.

<sup>a</sup> The spectral fitting results for the sources 5 and 6 could not be obtained because of a lack of counts.

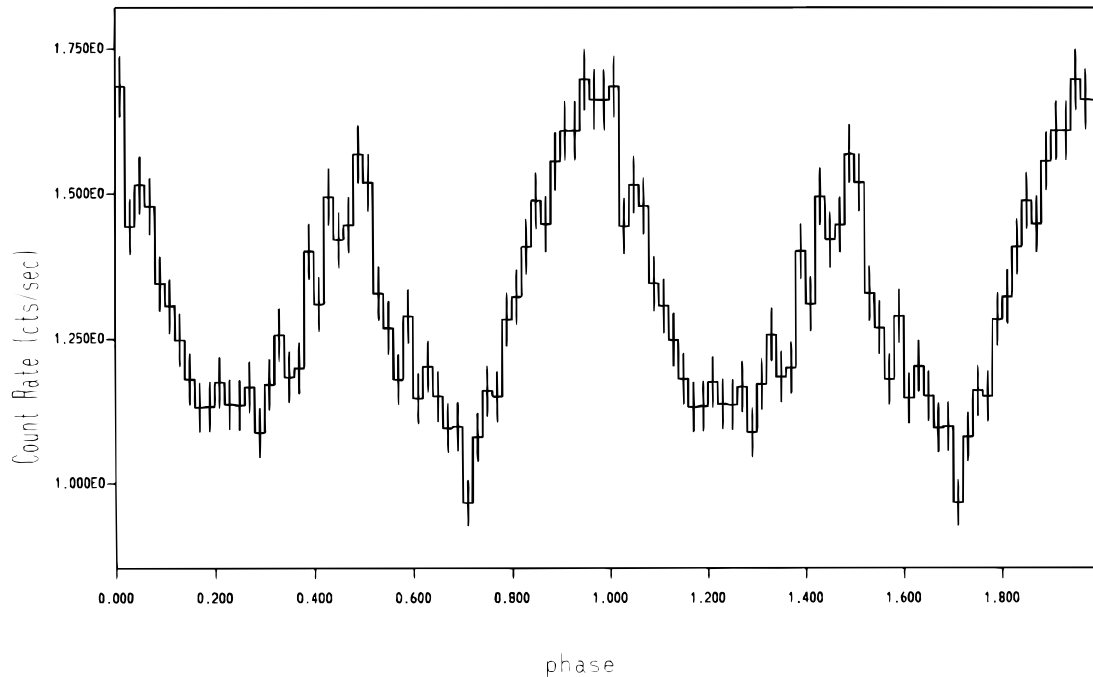


FIG. 9.—Pulse profile of 1E 2259 + 586 using PSPC

diffuse emission was used as a background. By virtue of their high  $N_H$ , sources 1 and 2 are probably background objects, and source 3 could be either a background object or part of the remnant. Source 4 is probably a foreground object, since it has a low  $N_H$ .

#### 4. DISCUSSION

Before being able to make inferences about the properties of the gas in CTB 109, we need to understand the origin of the various components. In the fits using coronal equilibrium models, the PSPC detects one ubiquitous component with  $kT \sim 0.2$  keV, plus a second one with  $kT \sim 0.56$  keV, restricted to the lobe and the northern and southern portions of the shell. The ambiguous BBXRT result, from a region in which the PSPC detects only one component, requires NEI conditions with a shock temperature of about 0.2 keV for the equipartition model or about 1.5 keV for nonequipartition. Given the uncertainties in the spectral fitting of both data sets, we conclude only that there is a real spectral difference in those regions where the PSPC requires a second component. If the equipartition model for the BBXRT data is the correct one, then we can further conclude that the plasma is not far removed from equilibrium and thus use the temperatures and emission measures inferred from the equilibrium model fits to make reasonable guesses about gas densities and masses.

There are two ways in which one can interpret the spectral difference. One is that the regions requiring two temperatures are farther removed from ionization equilibrium than the remainder of the remnant and have a characteristic temperature intermediate between the two values inferred from the equilibrium fit. Alternatively, the relative uniformity of the two temperatures suggests the possibility of two spatially distinct components, one ubiquitous, and one largely dominated to the lobe plus the northern and southern rims. As we discuss below, the similarity of the morphology of the region where the second component is required to the results of hydrodynamic simulations of

shock-cloud interactions provides a physical basis on which to expect two distinct sets of physical conditions.

##### 4.1. The Jetlike Lobe as Evidence for a Reflected Shock

To explain the origin of the jetlike lobe and its proximity to the X-ray pulsar, Gregory & Fahlman (1980, 1983) proposed a precessing jet model, analogous to SS 433 (Watson et al. 1983; Grindlay et al. 1983). According to this model, the lobe represents the hot gas of the precessing jet. The radio arc between the lobe and the pulsar also provided a clue that it may be related to the pulsar (Manchester 1987). We have found, however, that the X-ray emission from the lobe is thermal, contrary to the model prediction and in contrast to the nonthermal lobes in W50 (Yamauchi, Kawai, & Aoki 1994). We have also found no physical connection between the pulsar and the lobe using either these data or those from the *ROSAT* HRI (Hurford & Fesen 1995). Therefore, despite appearances, the jetlike lobe is probably not powered by or related to the central pulsar.

As discussed above, the similarity between the hardness ratio and spectral fit parameters of the lobe and the northern and southern shell segments suggests that they are physically related. The spectral similarity is one piece of evidence suggesting a relationship between these regions. More compelling is the morphological similarity between the surface brightness of the lobe plus shell segments (Fig. 2) and the plume structure in the models of SNR shocks reflected off molecular clouds (e.g., Tenorio-Tagle, Bodenheimer, & Yorke 1985). We suggest that the jetlike lobe has been produced by the interaction of the SNR with the molecular cloud. When an SNR shock encounters a large, dense obstruction in the ISM (such as a molecular cloud), it will propagate a forward shock into the obstruction (at much reduced velocity) as well as a reflected shock back into the rarefied medium behind it. The reflected shock propagates rapidly through the evacuated cavity of the remnant and causes a strong compression of the residual, low-density plasma. A Rayleigh-Taylor instability forms between the

cool, dense gas in the cavity and the hot, low-density plasma swept up by the reflected shock. The rapid growth of the Rayleigh-Taylor instability produces condensations that lag behind the reflected shock. The overall appearance of the reflected shock has been characterized by Tenorio-Tagle et al. (1985) as a “rising fireball moving away from the molecular cloud,” which also produces bright X-rays (Yorke et al. 1983; Yorke, Tenorio-Tagle, & Bodenheimer 1989; Tenorio-Tagle et al. 1985). The increased pressure at the cloud wall causes heating of the materials in the reverse flow with the dense materials, and thus the X-ray map reveals clearly a mushroom-shaped plume of X-ray emission that includes the lobe. Further supporting evidence for a significant shock-cloud interaction comes from the apparently enhanced X-ray emission at the interface between the SNR and the molecular cloud. The “bridge” between the pulsar and southern shell might be a part of this enhanced emission in projection. Also, the 60  $\mu$  IRAS map (Heydari-Malayeri et al. 1981) shows emission from the molecular cloud interaction sites and the lobe, supporting the idea of a connection between them.

A survey of the published simulations suggests that the most plausible scenario for CTB 109 is that its progenitor exploded 1–2 pc away from the edge of the giant molecular cloud. The models  $Z + 2$  or  $Z - \frac{1}{3}$  in Tenorio-Tagle et al. (1985) and HS 1 in Yorke et al. (1989), which most closely illustrate the SNR evolution when the progenitor explodes within a few parsecs from the interface between a molecular cloud and intercloud medium, reproduce with remarkable fidelity the morphology of CTB 109. The case  $Z - \frac{1}{3}$ , where the progenitor is barely embedded in the associated molecular cloud, and the  $Z + 2$  case, where the progenitor explodes 2 pc outside the cloud (Tenorio-Tagle et al. 1985) produces similar structures. In these cases, the center of divergence of the remnant’s velocity field moves away from the cloud because of the shock reflected from the cloud surface. The lobe appears to be perpendicular to the “bridge” of enhanced emission, which resembles the model of the interface between the molecular cloud and the SNR and the mushroom-like structure. The displacement of the pulsar by 3.6 (4.2 pc) can be explained by these models, as an alternative to a nonisotropic explosion (Hughes et al. 1981).

The above interpretation of the morphology of CTB 109 leads to a straightforward interpretation of the PSPC spectral map. The presence of the second component indicates those regions through which the reflected shock has propagated, forming the plume-shaped structure. The bulk of the remnant, requiring only a single component, is dominated material swept up by the original forward shock that has formed the hemispherical shell. It is unclear from our data

whether the plume is spatially distinct within the shell, and thus gas at two temperatures exists at different locations within the remnant, or whether the forward and reflected shock-heated material is intermixed, in which case the presence of the second component represents gas in a distinct ionization state.

#### 4.2. X-Ray Emitting Gas Properties

Whichever of the two conclusions we draw concerning the nature of the gas reheated by the reflected shock, its presence is irrelevant for making inferences about the global properties of CTB 109, as its overall dynamics and interaction with the ISM are dominated by the forward shock. If we assume that the gas is confined to a shell with a thickness of 20% of the remnant diameter (typical of the limb brightening observed in the PSPC image), then using the X-ray volume emission measure derived from the equilibrium fit in Table 3, we infer an average electron density of  $1.2^{+0.6}_{-0.2}$   $\text{cm}^{-3}$ , an X-ray emitting mass of  $440 M_{\odot}$ , and a total swept-up mass of  $420 M_{\odot}$ . While the western side, which is interacting with the molecular cloud, is probably in the radiative phase, most of the remnant is still in the adiabatic phase, and the standard Sedov solution can be used to estimate parameters. We infer a shock velocity  $v_s \sim 380 \text{ km s}^{-1}$  and an age of about  $1.9 \times 10^4$  yr using a temperature of  $kT_x = 0.17$  keV expected from the forward shock. The inferred supernova explosion energy is  $1.0 \times 10^{51}$  ergs, as shown in Table 3.

If we use instead the NEI fit results and assume they are applicable to the remnant as a whole, we infer the parameter values listed in Table 5, using equations (4a)–(4e) in HSC and assuming a distance to CTB 109 of 4 kpc. The equipartition fit gives an ionization age of  $17,000 \text{ cm}^{-3} \text{ yr}$ . It implies a blast-wave velocity of  $350 \text{ km s}^{-1}$ , an energy of  $1.5 \times 10^{51}$  ergs, and an age of  $2.1 \times 10^4$  yr. The ambient density is  $0.8 \text{ cm}^{-3}$ , and the swept-up mass is  $816 M_{\odot}$ . For the nonequipartition case, the model implies a blast-wave velocity of  $1100 \text{ km s}^{-1}$  and a considerably younger age of 6700 yr. The ambient density is  $0.08 \text{ cm}^{-3}$ . If multiple NEI components are present, then the high ionization age ( $n_0 t$ ) might be associated with denser, low shock temperature material we observe with the PSPC, and low ionization age with low density material with a high temperature, which may be recently reheated by the reflected shock.

The inferred remnant age and shock velocity from the PSPC data using an ionization equilibrium (CIE) model and from BBXRT data using an NEI model agree, despite the relatively low spectral resolution of the PSPC data and the localized coverage of the BBXRT data. The estimated energy is  $1.0 \times 10^{51}$  ergs for CIE model and  $1.5 \times 10^{51}$  ergs for NEI model, because the preshock density is  $0.6 \text{ cm}^{-3}$

TABLE 5  
THE BEST-FIT NONEQUILIBRIUM MODELS USING PSPC AND BBXRT

Parameter	$T_i \neq T_e$	$T_e = T_i$
$T_s$ .....	$10^{7.25}$ K	$10^{6.25}$ K
Distance (assumed).....	4 kpc	4 kpc
Radius .....	19 pc	19 pc
Angular diameter.....	34'	34'
Blast-wave shock velocity .....	$1100 \text{ km s}^{-1}$	$353 \text{ km s}^{-1}$
Energy (ergs).....	$1.5 \times 10^{51}$	$1.5 \times 10^{51}$
Age .....	6700 yr	$2.1 \times 10^4$ yr
Blast-wave mass .....	$85 M_{\odot}$	$816 M_{\odot}$
Hydrogen density of ambient medium.....	$0.08 \text{ cm}^{-3}$	$0.8 \text{ cm}^{-3}$

and  $0.8 \text{ cm}^{-3}$ , respectively. This difference comes from the fact that the excess density from the molecular interaction is not present in the regions to which the CIE model applied, while it is in the region observed by BBXRT. The fact that this excess density is not associated with the forward shock leads to incorrect values of other parameters when they are inferred from the BBXRT data based on formulae based on the Sedov solution. We thus believe that  $E = 1.0 \times 10^{51}$  ergs is a more correct value for explosion energy of CTB 109. Previous observations inferred different explosion energies: while Gregory & Fahlman (1980) inferred  $4 \times 10^{50}$  ergs, Morini et al. (1988) inferred  $2.3 \times 10^{51}$  ergs. Their result could also have been influenced by the presence of multiple components. Future high-resolution spectroscopic observations might reveal the presence of two distinct NEI components, one from forward shock and the other from the reverse flow.

#### 4.3. Interaction with the Molecular Cloud

One manifestation of the ongoing interaction between CTB 109 and the giant molecular cloud to the west is the anticorrelation between the brightness temperature of the CO arm crossing the northern half of the remnant and the X-ray surface brightness, as shown in Figure 2 of Tatematsu et al. (1987). The X-ray surface brightness of the CO arm is a factor of 3 lower than other faint parts of the remnant (e.g., region “F”). We consider three possible explanations for this.

First, the arm crosses in front of the remnant, and the anticorrelation is the result of differential absorption. Second, the molecular cloud encounter reduces the shock velocity, and thus the gas is slightly cooler than in neighboring regions. Third, the X-ray emitting gas in the direction of the CO arm has either a smaller emission column or a lower density, resulting in reduced emission measure. We can rule out this latter possibility, as the emission measure of the arm is not appreciably less than its surroundings. Thus, if the CO arm does extend into the remnant and reduce the X-ray emission column, then the gas in the column must be denser than average to compensate.

As can be seen in Figure 8 (*bottom*), region “D,” which includes the CO arm, has neither a higher  $N_H$  value nor a lower temperature than elsewhere. However, the low- $E$  cut spectral hardness map (Fig. 4, *bottom*) shows that the emission along the CO arm is harder than its surroundings. To quantify more carefully the spectral difference between this region and its surroundings, we extracted a spectrum from the CO peak region confined by an ellipse of major and minor axes  $5''.2$  and  $4''$ , where the low- $E$  cut hardness map shows hard emission.

For this region (“CO peak” in Table 2), we find  $N_H = 1.1 \pm 0.1 \times 10^{22} \text{ cm}^{-2}$ , marginally higher than its surroundings, and  $kT = 0.18 \pm 0.05 \text{ keV}$ , marginally lower. If the lower X-ray surface brightness is due to foreground absorption alone, then a minimum column density of about  $1.25 \times 10^{22} \text{ cm}^{-2}$  is required. For comparison, converting the CO column density to H I column density gives an  $N_H$  value of  $(0.07\text{--}0.1) \times 10^{22} \text{ cm}^{-2}$  for the arm (Tatematsu et al. 1987), consistent with and no higher than the  $N_H$  excess obtained by the fit. From this we conclude that the reduced surface brightness can be due only in part to excess  $N_H$ ; an intrinsic lack of X-ray emission as a consequence of the shock-cloud encounter cannot be ruled out.

Tatematsu et al. (1987) argued that the bright X-ray lobe

is an artifact of shadowing produced by the higher column density within the arm. This is clearly not the case, for two reasons. Shadowing only partially accounts for the surface brightness difference, and, as we have shown above, the lobe has an extra emission component that accounts for some of the surface brightness difference.

#### 5. SUMMARY

Using *ROSAT* PSPC data we have performed the first spatially resolved X-ray spectroscopic mapping of CTB 109. The PSPC spectra have been supplemented with BBXRT spectra of 1E 2259+586 and nearby diffuse emission. We summarize our significant new results.

1. The PSPC reveals clear spectral variations across the remnant. The column density gradually decreases from the northeast to the southwest, largely consistent with the low-energy (0.7 keV) cut hardness map. The spectrum over most of the shell is well fitted by a one-temperature coronal equilibrium plasma. However, for the lobe and the northern and southern shell segments a two-component thermal model is required, suggesting the plasma in these regions is farther from ionization equilibrium than elsewhere in the remnant. These results imply variation of ionization state across the remnant. The higher  $N_H$  value of the spectrum of the CO peak region indicates that the reduced X-ray surface brightness is partially, but not entirely, due to absorption.

2. The fact the X-ray emission from the lobe is thermal indicates that the lobe is probably not powered by the central pulsar. The spectral similarity of the lobe to the northern and southern segments of the shell and the morphological similarity of the three regions to hydrodynamical models (Tenorio-Tagle et al. 1985) support the idea that the lobe is part of a larger, plumelike structure formed by the interaction between a reflected shock from the SNR–molecular cloud collision and gas in the SNR interior.

3. The simultaneous fit of PSPC and BBXRT spectra of a region in the interior of the remnant just south of the pulsar has confirmed that the plasma there has not reached ionization equilibrium. A single-component ionization nonequilibrium model adequately fits the spectra. Acceptable fits can be found for both electron-ion equipartition and non-equipartition. The best fit for  $T_e \neq T_i$  is shock temperature  $T_s = 2 \times 10^7 \text{ K}$ , ionization parameter  $\eta = 10^{49} \text{ ergs cm}^{-6}$ , and ionization age  $n_0 t$  of  $430 \text{ cm}^{-3} \text{ yr}$ . For  $T_i = T_e$ ,  $T_s = 1.8 \times 10^6 \text{ K}$ ,  $\eta = 10^{51} \text{ ergs cm}^{-6}$ , and  $n_0 t = 17,000 \text{ cm}^{-3} \text{ yr}$ . For the nonequipartition case ( $T_e \neq T_i$ ) the plasma is far removed from ionization equilibrium.

4. We have detected extended emission with a non-thermal spectrum around the pulsar 1E 2259+586 using the PSPC and HRI images. This emission most likely arises from a compact synchrotron nebula rather than a dust-scattering halo, because its spectrum is not significantly softer than that of the pulsar. The pulsar shows a period  $6.978814 \pm 9.4 \times 10^{-6} \text{ s}$ , and its constant  $\dot{P}$  is consistent with that measured by *ASCA*.

The authors thank A. Baykal, J. H. Swank, R. Corbet, and D. Finley for helpful discussions regarding the pulsar. We acknowledge A. Szymkowiak for assistance with the ionization nonequilibrium model computation and J. Ballet for useful comments on the manuscript. We also express our gratitude to the referee, K. Koyama, for his insightful comments.

## REFERENCES

- Bevington, P. R., & Robinson, D. K. 1969, *Data Reduction and Error Analysis for the Physical Science* (New York: McGraw-Hill)
- Blair, W. P., & Kirshner, R. P. 1981, *Nature*, 291, 132
- Corbet, R. H. D., Smale, A. P., Ozaki, M., Koyama, K., & Iwasawa, K. 1995, *ApJ*, 443, 786
- Davies, S. R., Coe, M. J., Payne, B. J., & Hanson, C. G. 1989, *MNRAS*, 237, 973
- Fahlman, G. G., Hickson, P., & Richer, H. B. 1982, *ApJ*, 261, L1
- Fesen, R. A., & Hurford, A. P. 1995, *AJ*, 110, 747
- Giovanelli, R., & Haynes, M. P. 1979, *ApJ*, 230, 540
- Gorenstein, P., & Tucker, W. H. 1976, *ARA&A*, 14, 373
- Gregory, P. C., Braun, R., Fahlman, G. G., & Gull, S. F. 1983, in *Supernova Remnants and Their X-Ray Emission*, ed. J. Danziger & P. Gorenstein (Dordrecht: Reidel), 437
- Gregory, P. C., & Fahlman, G. G. 1980, *Nature*, 287, 805
- . 1983, in *Supernova Remnants and Their X-Ray Emission*, ed. J. Danziger & P. Gorenstein (Dordrecht: Reidel), 429
- Grindlay, J. E., Band, D., Seward, F., & Stella, L. 1983, in *Supernova Remnants and Their X-Ray Emission*, ed. J. Danziger & P. Gorenstein (Dordrecht: Reidel), 459
- Hamilton, A. J., Sarazin, C. L., & Chevalier, R. A. 1983, *ApJS*, 51, 115 (HSC)
- Harnden, F. R., Grant, P. D., & Seward, F. D. 1985, *ApJ*, 299, 828
- Heydari-Malayeri, M., Kahane, C., & Lucas, R. 1981, *Nature*, 293, 549
- Hughes, V. A., Harten, R. H., Costain, C. H., Nelson, L. A., & Viner, M. R. 1984, *ApJ*, 283, 147
- Hughes, V. A., Harten, R. H., & van den Bergh, S. 1981, *ApJ*, 246, L127
- Hurford, A. P., & Fesen, R. A. 1995, *MNRAS*, 277, 549
- Iwasawa, K., Koyama, K., & Halpern, J. 1992, *PASJ*, 44, 9
- Koyama, K., Hoshi, R., & Nagase, F. 1987, *PASJ*, 39, 801
- Koyama, K., et al. 1989, *PASJ*, 41, 461
- Manchester, R. N. 1987, *A&A*, 171, 205
- Mathis, J. S., & Lee, C. W. 1991, *ApJ*, 376, 490
- Middleditch, J., Pennypacker, C. R., & Burns, M. S. 1983, *ApJ*, 274, 313
- Morini, M., Robba, N. R., Smith, A., & Van der Kris, M. 1988, *ApJ*, 333, 777
- Predehl, P., & Schmitt, J. H. M. M. 1995, *A&A*, 293, 889
- Raymond, J. C., & Smith, B. W. 1977, *ApJS*, 35, 419
- Rho, J.-H., Petre, R., Schlegel, E. M., & Hester, J. J. 1994, *ApJ*, 434, 757
- Safi-harb, S., Ogelman, H., & Finley, J. P. 1995, *ApJ*, 439, 722
- Serlemitsos, P. J., et al. 1992, in *Frontiers of X-Ray Astronomy*, ed. Y. Tanaka & K. Koyama (Tokyo: Universal Acad.), 221
- Seward, F., & Harnden, F. R. 1982, *ApJ*, 256, L45
- Sharpless, S. 1959, *ApJS*, 41, 257
- Shklovsky, I. S. 1968, *Supernovae* (London: Wiley)
- Sofue, Y., Takahara, F., & Hirabayashi, H. 1983, *PASJ*, 35, 447
- Tatematsu, K., Fukui, Y., Nakano, M., Kogure, T., Ogawa, H., & Kawabata, K. 1987, *A&A*, 184, 279
- Tatematsu, K., Nakano, M., Yoshida, S., Wiramihardja, S. D., & Kogure, T. 1985, *PASJ*, 37, 345
- Tatematsu, K., Fukui, Y., Iwata, T., Seward, F. D., & Nakano, M. 1990, *ApJ*, 351, 157
- Tenorio-Tagle, G., Bodenheimer, P., & Yorke, H. W. 1985, *A&A*, 145, 70
- Watson, M. G., Willingale, R., Grindlay, J. E., & Seward, F. D. 1983, *ApJ*, 273, 688
- White, N. E., Angelini, L., Ebisawa, K., Tanaka, Y., & Ghosh, P. 1996, *ApJL*, 463, L83
- Yamauchi, S., Kawai, N., & Aoki, T. 1994, *PASJ*, 46, L109
- Yorke, H. W., Tenorio-Tagle, G., & Bodenheimer, P. 1983, in *Supernova Remnants and Their X-Ray Emission*, ed. J. Danziger & P. Gorenstein (Dordrecht: Reidel), 393
- Yorke, H. W., Tenorio-Tagle, G., Bodenheimer, P., & Rozyczka, M. 1989, *A&A*, 216, 2071